NANO LETTERS

Letter

pubs.acs.org/NanoLett

Growth Conditions Control the Elastic and Electrical Properties of ZnO Nanowires

Xiaoguang Wang,[†] Kai Chen,[†] Yongqiang Zhang,[†] Jingchun Wan,[†] Oden L. Warren,[‡] Jason Oh,[‡] Ju Li,[†,§] Evan Ma,[†,∥] and Zhiwei Shan*[,†]

[†]Center for Advancing Materials Performance from the Nanoscale (CAMP-Nano) & Hysitron Applied Research Center in China (HARCC), State Key Laboratory for Mechanical Behavior of Materials, Xi'an Jiaotong University, Xi'an 710049, P. R. China

[‡]Hysitron Incorporated, 9625 West 76th St, Minneapolis, Minnesota 55344, United States

[§]Department of Nuclear Science and Engineering and Department of Materials Science and Engineering, Massachusetts Institute of Technology, Cambridge, Massachusetts 02139, United States

[∥]Department of Materials Science and Engineering, The Johns Hopkins University, Baltimore, Maryland 21218, United States

S *Supporting Information*

ABSTRACT: Great efforts have been made to synthesize ZnO nanowires (NWs) as building blocks for a broad range of applications because of their unique mechanical and mechanoelectrical properties. However, little attention has been paid to the correlation between the NWs synthesis condition and these properties. Here we demonstrate that by slightly adjusting the NW growth conditions, the cross-sectional shape of the NWs can be tuned from hexagonal to circular. Room temperature photoluminescence spectra suggested that NWs with cylindrical geometry have a higher density of point defects. In situ transmission electron microscopy (TEM) uniaxial tensile-electrical coupling tests revealed that for similar diameter, the Young's modulus and electrical resistivity of hexagonal NWs is always larger than that of cylindrical NWs, whereas the piezoresistive coefficient of cylindrical NWs is generally higher. With decreasing diameter, the Young's modulus and the resistivity of NWs increase, whereas their piezoresistive coefficient decreases, regardless of the sample geometry. Our findings shed new light on understanding and advancing the performance of ZnO-NW-based devices through optimizing the synthesis conditions of the NWs.

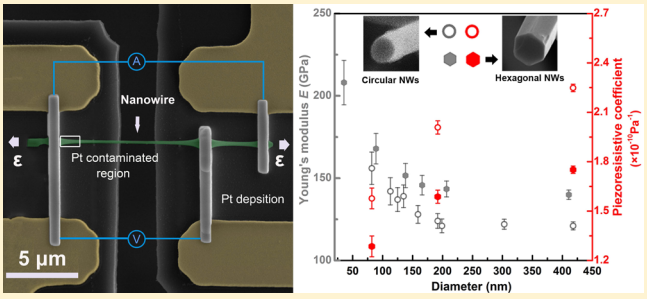

KEYWORDS: *ZnO nanowires, in situ TEM uniaxial tensile-electrical coupling test, Young's modulus, piezoresistivity, shape effect, point defects*

Zinc oxide nanowires (ZnO NWs) have attracted worldwide interest for their promising application in piezoelectric devices and sensors.[1−8] In order to optimize the working condition and improve the reliability of these devices, it is paramount to fully understand the elastic and mechanoelectrical properties of individual ZnO NWs. However, comprehensive literature survey indicated that the piezoresistive property of individual ZnO NW has been rarely studied quantitatively. And even for the most fundamental parameter of Young's modulus, the reported data[9−20] are far from consistent and can be classified into three types of behaviors. Type I is size-strengthening. In 2006, Chen et al.[9] reported that when the sample size was reduced from 220 to 50 nm, the Young's modulus of ZnO NWs will increase from 140 to 220 GPa. A similar trend was reported by Agrawal et al.[10] in 2009. Type II is size-independent. By employing an AFM lateral bending technique, Wen et al.[14] reported in 2008 that the modulus of ZnO NWs is diameter independent and close to the bulk value even for sample diameter down to 18 nm. Type III is that the elastic moduli of ZnO nanostructures are much lower than the ZnO bulk value, which implies a size-weakening effect. In 2009, Zhao and Mao[15] reported that the Young's modulus of ZnO nanobelt is about 40 GPa in dark environment. The much lower modulus was in agreement with that reported by Bai et al.[19] in 2003. It was interesting to note that all three types of results were reported in Physical Review Letters. The obvious discrepancies suggest that there could be factors that should be considered in measuring the Young's modulus of ZnO NWs but unfortunately were overlooked in previous works.

In order to uncover the hidden factors, we summarize the reported data on the modulus of ZnO nanostructures in Table 1. Detailed analysis suggests that the inconsistency may mainly come from two sources. First, uncertainties resulting from the intrinsic limitation of various testing protocols. Take indentation test, for example, even though it is an efficient and useful

Received: July 20, 2015
Revised: October 15, 2015
Published: October 28, 2015

DOI: 10.1021/acs.nanolett.5b02852
Nano Lett. 2015, 15, 7886−7892

Table 1. Summary of the Experimental Reported Data on the Modulus of ZnO Nanostructures

types	Young's modulus [GPa]	diameter [nm]	test methods	shape
Type I: size strengthening	**140−220**	**550−17**	in situ **SEM resonance**[9]	**circular**
	142−160	413−20	in situ TEM tension[10]	hexagonal
	150−210	250−20	in situ SEM tension[11]	[a]
	140−170	80−20	AFM cantilever in situ SEM tension[12]	[a]
	140−210	80−20	AFM cantilever in situ SEM buckling[12]	[a]
	104−198	134−25	contact resonance AFM[13]	[a]
Type II: size independent (like bulk)	**140**	**340−18**	**AFM three point bending**[14]	**circular**
Type III: much lower than their bulk value	**40**		**AFM nanoindentation**[15]	**nanobelts**
	38.2 ± 1.8		AFM three point bending[16]	nanobelts
	29 ± 8	45	AFM bending[17]	[a]
	21	314−217	in situ SEM tension[18]	[a]
	52		in situ TEM resonance[19]	nanobelts

[a]The cross-sectional shape of NWs not shown in paper.

tool to get the relative modulus evolution, the complex stress/strain conditions as well as the bulk-materials-based empirical formula make it more challenging to get an absolute modulus of nanostructured materials convincingly. For flexural loading tests, that is, bending[14,20,21] or resonance,[9,19] the measured modulus will be inversely proportional to the fourth power of the measured diameter. This means that small measurement error can result in large deviation of the measured modulus, especially for those NWs with tiny diameters. In addition, surface effects are expected to be more pronounced under flexural loading than those under uniaxial loading.[12] What is more, although resonance is a well-accepted approach, uncertainty in the boundary condition could introduce considerable errors to the Young's modulus measurement.[22] The nonuniform stress distribution of the flexural loading will further complicate the analysis of the experimental results. Uniaxial tension, on the other hand, is more straightforward and reliable, as the stress in the specimen tends to be more uniform.[10,23,24] The challenge for tensile test is to measure the elastic strain with high accuracy. Second, even though the samples used by different research groups had been synthesized with different methods, little attention has been paid to link the ZnO properties to their sample conditions other than the crystal structure and orientation. Other factors that are very likely to play a key role in affecting the properties of ZnO NWs include the chemical composition,[25] cross-sectional geometry,[26] internal defects,[27] and so forth. For example, cylindrical NWs were used by Wen et al.,[9] whereas Agrawal et al.[10,23] studied hexagonal NWs, but the effect of the cross-sectional geometry difference had been pretty much overlooked in these studies.

In this work, we fabricated cylindrical and hexagonal ZnO NWs by adjusting the growth condition slightly. Photoluminescence (PL) spectrum suggests that the internal defect density is higher in cylindrical ZnO NWs. By adopting a state-of-the-art *in situ* transmission electron microscope (TEM) uniaxial tensile-electrical coupling testing technique,[28] the size and cross-sectional geometry dependence of the elastic modulus and piezoresistive coefficient of the as-synthesized NWs are unambiguously revealed. Our findings are expected to clarify the long-existing conflicts about the elastic properties of ZnO NWs and to shed new light on the rational design and fabrication of ZnO NW based devices.

As shown in Figure 1a, the NWs fabricated at high flow rate were almost parallel to the surface of the Si substrate (Figure 1a), and displayed roughly circular cross-section (inset of Figure 1a), whereas the ones under low flow rate oriented largely vertical to the Si substrate surface and showed hexagonal cross-section (inset of Figure 1b). The Au-nanoparticle catalysts were always found at one end of the cylindrical ZnO NWs (Figure. 1a), suggesting that the growth process followed the classic vapor−liquid−solid (VLS) mechanism.[29,30] In contrast, no catalyst particles were observed on the tip of hexagonal NWs but a thin ZnO film was found on the substrate surface (Figure 1b). Therefore, the growth of the hexagonal ZnO NWs is very likely following a self-seeding vapor−solid (VS) mechanism.[31] On average, the length and diameter of the hexagonal ZnO NWs were larger than those of the cylindrical NWs after growing at the identical temperature (925 °C) for 20 min. Selected area electron diffraction (SAED) and X-ray diffraction patterns confirmed that both types of NWs were single crystalline with hexagonal wurtzite structure and no significant difference was observed from the diffraction peak width or intensity.

The chemistry and defects of both types of NWs were also characterized. No impurity elements were detected in the NWs from energy dispersive X-ray spectroscope analysis. However, distinctly different PL spectra were obtained from cylindrical and hexagonal NWs using a Xe excitation light source with the wavelength of 340 nm. Both spectra contained two main bands, a narrow one with the peak maximum at 3.2 eV attributable to the near band-edge emission (NBE) and a green luminescence (GL) with peak maximum around 2.45 eV from the defect centers.[32] In order to examine the GL carefully, the peaks of the NBE in both spectra were normalized and plotted in Figure 1c. Obviously, the GL peak of cylindrical NWs is much higher than that for hexagonal NWs.

For the mechanical−electrical coupling tests, the ZnO NWs were transferred and welded onto a Si-based MEMS mechanoelectrical testing device, E-PTP (Figure 2a), inside a dual beam focused-ion beam system, with the method similar to the one reported in previous literature.[33,34] As shown in Figure. 2a, a three-probe configuration was employed. With less Pt pollution/damage, this easy-to-fabricate and spatially efficient approach is equivalent to the conventional four-probe method (Figure S1 in Supporting Information), and thus the contribution of the resistance from the contacts and circuit can be minimized. E-beam induced deposition was taken as the first option to connect the NW to the Au electrodes for resistivity measurement to minimize the damage of the ion beam (i-beam). The $I-V$ curve under this condition, however, exhibited rectifying characteristics (Figure 2b, upper). The nonlinear nature is typical of Schottky contact for the metal−

DOI: 10.1021/acs.nanolett.5b02852
Nano Lett. 2015, 15, 7886−7892

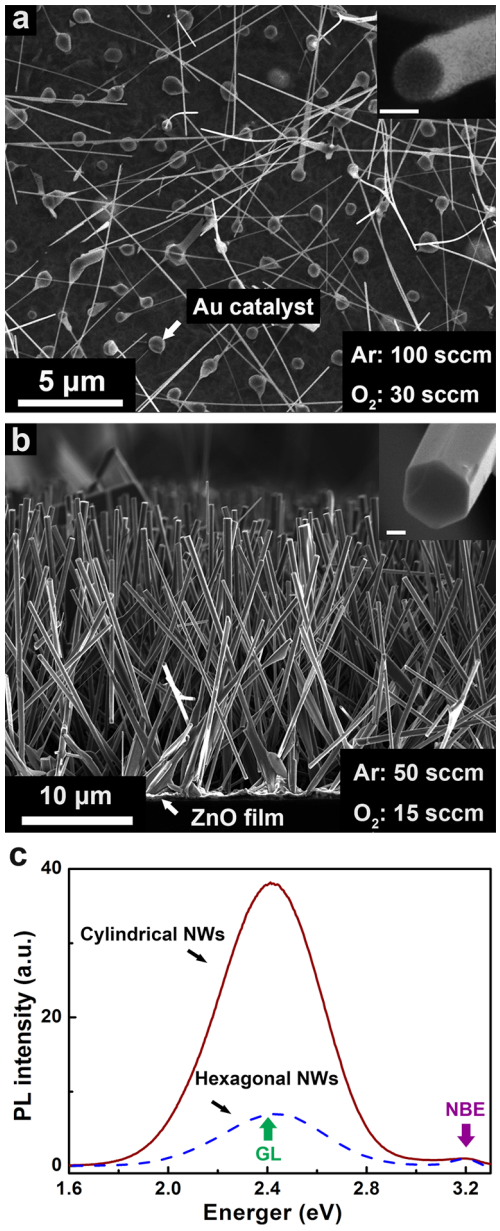

Figure 1. SEM and PL spectra of the cylindrical and hexagonal ZnO NWs, respectively, synthesized at different carrier gas flow rate. (a) SEM top view of the cylindrical NWs grown under higher carrier gas flow rate. The inset shows the circular morphology of the NW cross-section. (b) Side-view SEM image of hexagonal ZnO NWs synthesized under low carrier gas flow rate. The inset shows a high magnification SEM picture of the hexagonal cross-section of a NW. The inset scale bars in both (a) and (b) represent 100 nm. (c) Room temperature PL spectra for both types of ZnO NWs. The higher green luminescence intensity from the cylindrical NWs indicates a higher density of defects.

semiconductor junction. To study the intrinsic electrical transport properties, ohmic contact is highly desirable. Interestingly, we found i-beam-induced Pt deposition exhibited perfect ohmic contact, as shown in Figure 2b (lower, red). Presumably, this is due to the fact that part of the high energy Ga ions were directly injected into the ZnO NWs, which increases defect-assisted tunneling across the Schottky barrier[35] and improves the electrical contact.[36] Therefore, i-beam-induced deposition was always employed to fabricate the microleads for all the mechanical, electrical, and mechano-electric properties measurements in this study. To minimize the i-beam radiation damage, only the welded parts of the NW were exposed to the i-beam during the whole process. As shown in Figure. 2a, the welded spots were about 1 μm wide. It is worth mentioning that the NW close to the weld points is often "polluted" by the diffusive Ga and Pt. The polluted length measured from SEM image was about 1−2 μm (marked by the white square in Figure 2a) next to the welding areas. Outside the affected region, the NWs appeared clean, especially the part in between the trench of the PTP, which has been used to measure the Young's modulus.

The electrical resistance was measured under sweeping voltage mode both outside and inside a TEM to evaluate the environmental effects. As shown in Figure 2c, the resistance was stable in air. However, once the prevacuum chamber was pumped, the resistance began to decrease until reaching a stable value. More interestingly, as soon as the NW was irradiated with the high energy TEM e-beam, the resistance began to drop again until an even lower constant value was obtained, given the fixed TEM e-beam intensity. The environment-dependent resistivity probably resulted from the change in the depletion layer under the NW surface as the number of chemisorbed oxygen and vapor species varies at different pressure levels[37,38] and upon e-beam irradiation.[39] Previous studies[40,41] also demonstrated that pressure, electron beam irradiation, and humidity can all affect the measured elastic modulus of NWs and, therefore, contribute significantly to the large scattering in previously measured elastic modulus in ZnO nanowires. So, in order to eliminate or minimize the environmental effects, all the properties reported in this study were measured after the stabilization under evacuation and e-beam irradiation.

For accurate measurement of electrical resistivity, $I-V$ curve was obtained by sweeping the voltage V from −2 to 2 V and recording the electrical current I simultaneously. Then the electrical resistivity, ρ, was calculated from measuring the resistance R (which equals to the slope of the linear $I-V$ curve) and the dimensions of the NW. For similar sample diameter, the resistivity of hexagonal NWs is typically 3 orders of magnitude higher than that of cylindrical ones, as shown in Figure 2d. A size dependence is also observed, according to the fact the resistivity increases by about 40% for both types of NWs as the diameter decreases from ∼420 to ∼80 nm.

The in situ tensile test was realized by using a Hysitron PicoIndenter (PI95) TEM holder[42,43] inside a JEOL 2100F TEM. By measuring the distance and displacement between two tiny carbon markers (indicated by the black arrows in Figure 3a) before and during the tensile test, the elastic strain loaded on the NW at the gauge part can be calculated precisely. In this study, the mechanical tests were carried out under displacement rate control, and the stress on the NW was measured to be linearly proportional to time, indicating an elastic deformation behavior. A typical engineering stress−strain curve of a cylindrical ZnO NW is shown in the inset of Figure 3b. The curve shows good linearity in the whole stage of loading, indicating that our study was in the elastic region, which is further confirmed by no detectable hysteresis in the force−strain curve in multiple loading−unloading tests. The Young's modulus E was measured from the slope of the stress−strain curve, and the propagated uncertainty was estimated by considering the errors in the measurement of diameter, force, and displacement. The measured moduli are plotted in Figure 3b as a function of effective diameter, which is defined as $d \equiv$

DOI: 10.1021/acs.nanolett.5b02852
Nano Lett. 2015, 15, 7886−7892

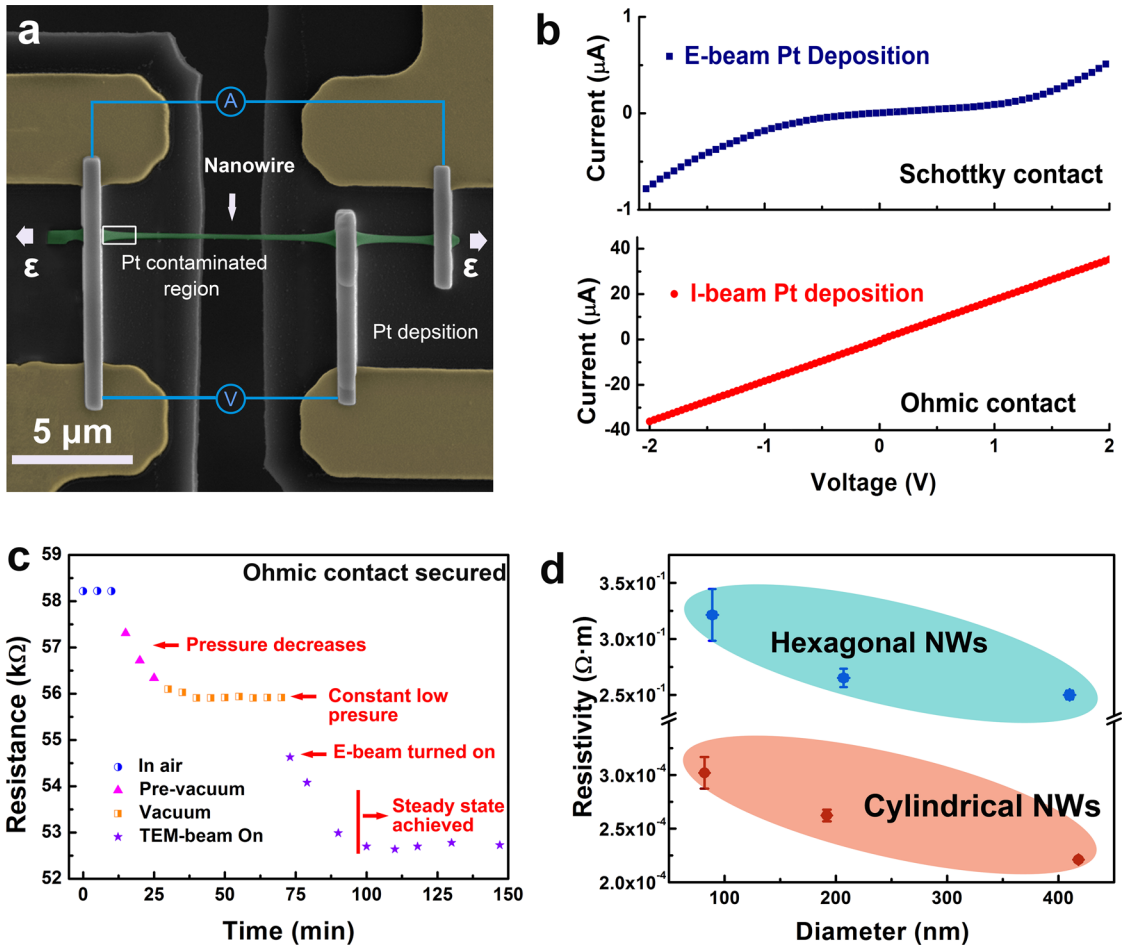

Figure 2. Experiment setup and electrical measurement of individual ZnO NWs. (a) SEM image demonstrating the three-probe method for electrical and piezoelectric measurements of ZnO NWs. (b) The $I-V$ curves of an as-grown cylindrical ZnO NW with Pt microleads deposition induced by e-beam (top) and i-beam (bottom), suggesting Schottky and Ohmic contact, respectively. (c) Electrical resistance evolution of an individual ZnO NW as the sample was inserted into a TEM. (d) Effective diameter dependence of electrical resistivity of cylindrical and hexagonal ZnO NWs without any intentionally applied strain. The resistivity of the hexagonal NWs is 3 orders of magnitude higher than the one of the cylindrical NWs.

$(4A/\pi)^{1/2}$, where A is the measured cross-sectional area. For both hexagonal and cylindrical NWs, E increases significantly as the diameter decreases below 150 nm, similar to the size-strengthening effect reported by previous studies.[9,10] The difference is that a strong cross-sectional shape effect of the modulus can be concluded from Figure. 3b. Taking the error bars into account, the Young's modulus of a hexagonal ZnO NW is remarkably higher than a cylindrical NW with the same effective diameter in the measured size range. When the diameter is greater than 200 nm, the Young's modulus of the hexagonal NWs is approximately 140 GPa, which is consistent with the reported bulk modulus at room temperature,[10] whereas the one of a cylindrical NW is about 13% lower.

The electrical resistivity was studied as a function of elastic strain. One typical example is shown in Figure. 4. The current I passing through an individual NW was recorded while sweeping the voltage from −5 to 5 mV at fixed strain levels of 0%, 0.63%, 1.28%, and 1.87%, respectively (inset in Figure. 4a). After recording the $I-V$ curve at each nonzero strain, the strain was unloaded and the $I-V$ sweep was repeated. The fact that the resistance could return to the initial strain-free value indicates that the observed resistivity evolution result from elastic strain. As tensile elastic strain increases, the slope of the $I-V$ curve turns steeper, suggesting that the resistivity goes down (the inset in Figure 4a). This phenomenon was further confirmed by measuring the electrical current I during the tensile loading of a NW, on which a constant low voltage (5 mV) was applied in order to reduce the joule heating. As shown in Figure 4b, the electrical current responded simultaneously to the elastic strain and returned to the initial value when the force was unloaded. It is noted that during this test, the stress was programmed to keep at 1.5 GPa for 20 s; however, due to the drift of the picoindenter, the tensile stress loaded on the sample decreased gradually. Meanwhile, the resistivity increased accordingly, which indicated that resistivity strongly depended on stress and elastic strain, and the dependence could be detected sensitively via our method. Three loading−unloading cycles were performed, and the results were reproducible, indicating good stability and reliability of our three-probe approach, and thus the observation is truly from the elastic strain-induced electrical transport property evolution.

In principle, the electrical properties of a semiconductor lacking an inversion symmetry can be engineered by strain possibly due to two effects: piezoelectricity and piezoresistivity.[3,44] In our study, good ohmic contacts were secured and retained so the piezoelectric potential could not be accumulated in the closed circuit. Moreover, the observed symmetric shape of the $I-V$ curve under strain in the inset of Figure 4a is also

DOI: 10.1021/acs.nanolett.5b02852
Nano Lett. 2015, 15, 7886−7892

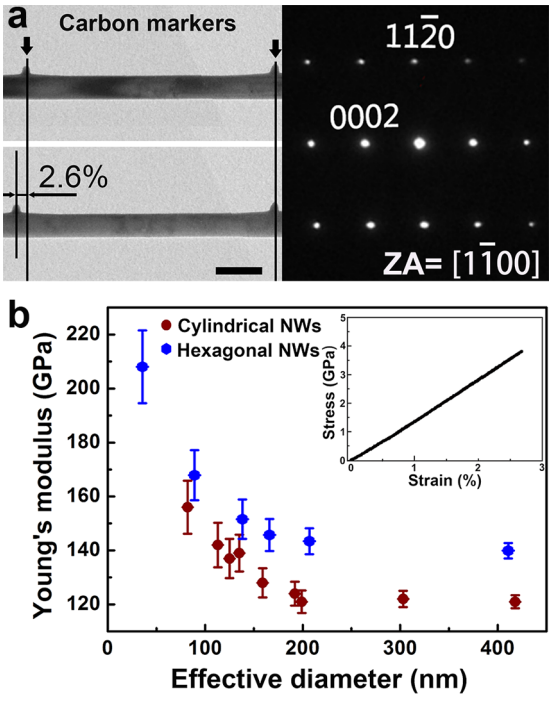

Figure 3. Young's modulus of ZnO NWs as a function of effective diameter and cross-sectional morphologies. (a) Uniaxial tensile strain measurement from the displacement of carbon markers. SAED pattern indicates that the single crystal ZnO NW grew in [0001] direction. (b) Variation of Young's modulus with effective diameter and cross-sectional shape. The inset is a stress vs strain curve response for a cylindrical NW. The scale bars in (a) represent 200 nm.

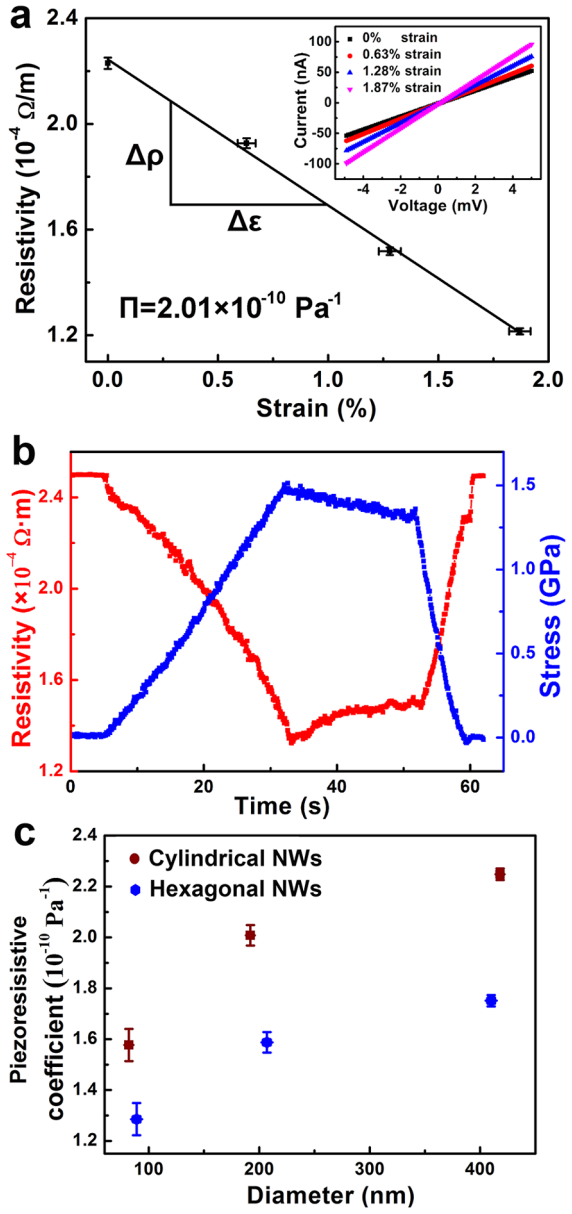

Figure 4. Piezoresistivity of ZnO NWs with different size and cross-sectional morphologies. (a) Linear resistivity drop as the uniaxial tensile strain increases, measured on a cylindrical ZnO NW. Inset is the $I-V$ curves of the same NW under various strains. (b) Resistivity response under applied stress in real time. (c) Piezoresistive coefficient of both types of NWs with different effective diameters.

contrary to what was reported on the piezoelectric effect of ZnO NWs.[3] Therefore, in our study, piezoelectricity is excluded, and the effect observed here should be due to piezoresistivity. Theoretically, piezoresistivity can result from the strain-induced band gap variation, which affects the concentration of the charge carriers, the band curvature change, which alters the effective mass and mobility of the charge carriers, and, for materials at the sub-10 nm scale, the quantization effect that occurs in the first few atomic layers.[45] Given the fact that the diameter of the NW in our study (>80 nm in diameter) is in the regime that the quantum confinement is negligible,[45] the resistivity decrease is most likely due to the intrinsic band structure change induced by strain. To quantify the strain effect on resistivity, the piezoresistive coefficient Π is defined as

$$\Pi \equiv -\frac{\Delta\rho/\rho_0}{\sigma} = -\frac{\rho - \rho_0}{\varepsilon \cdot E \cdot \rho_0}$$

where ρ_0 and ρ are the electrical resistivity of the NW at zero stress and stress σ, respectively. The piezoresistive coefficient of six NWs with different diameters and cross-sectional shapes was measured and displayed in Figure 4d. It can be seen that Π for cylindrical NWs is generally higher than that for hexagonal ones for similar diameter, and for both types of NWs, Π decreases as the diameter decreases (Figure 4c).

As shown in Figure 1c, the PL spectrum measurements unambiguously demonstrated the different GL intensity in the two types of the ZnO NWs. A correlation was proposed half a century ago between the GL and electron paramagnetic resonance attributed to oxygen vacancies in reduced ZnO.[46,47] After that, Vanheusden et al.[48,49] proved that the GL emission resulted from the recombination of a photogenerated hole with a singly ionized oxygen vacancy. Although we could not exclude other point defects,[32,50] there is strong evidence that oxygen vacancy might be responsible for the GL band in ZnO.[46−49,51−54] The prominent GL intensity undoubtedly indicates higher concentration of defects in the as-grown cylindrical ZnO NWs than in the hexagonal ones, dictated by the growth conditions. What is more, earlier experimental and theoretical studies also indicated that native oxygen vacancies could also impact the electrical transport properties of ZnO, by generating high levels of unintentional n-type dopants.[55,56] Therefore, the cylindrical ZnO NWs could be regarded as a more heavily doped, and thus a more

DOI: 10.1021/acs.nanolett.5b02852
Nano Lett. 2015, 15, 7886−7892

electrically conductive, n-type semiconductor than the lighter doped hexagonal ones.

When oxygen vacancies are introduced into materials, the charge neutrality is restored by electrons localizing around the cations to form lower-valence cations defects. As a result, the vacancies will increase average bond length and, thus, result in a reduction in the intrinsic elastic modulus.[57] Recently, simulation and experimental studies have revealed in several materials that point defects could strongly influence the mechanical properties such as Young's modulus.[50,57−62] Pan et al. applied first-principles density functional theory calculations and found that the calculated Young's modulus of ReB_2 with 1.3% concentration of boron vacancies (415 GPa) is much lower than that (698 GPa) of the defect-free one. Wang et al. observed the decrease of elastic modulus in pure and gadolinium-doped ceria as the oxygen vacancy concentration increases by conducting nanoindentation tests.[63] Analogously, we propose that the higher density of point defects in cylindrical ZnO NWs was partially responsible for the lowered Young's modulus.

The increase of the Young's modulus as the diameter shrinks has been explained by core−shell models even though different cross-sectional geometry was being used in these studies.[9,11] The apparent modulus was attributed to an average of the stiffened surface layer with higher effective modulus E_S and the relatively lower core modulus E_c. The fact that the resistivity increases with decreasing NW diameter suggests that the density of point defects (that gives unintentional n-doping) is lower in the NWs with smaller diameter, which may be another factor affecting the size effect on Young's modulus. In our study, the modulus begins to increase significantly when the NW diameter decreases to 140 nm, which is different from what was reported by He et al. (120 nm)[11] or Agrawal et al. (80 nm).[10] The difference may arise from the fact that surface stress effect[64] is not only affected by diameter but also by the cross-sectional geometry. In general, we propose the discrepancy comes from the difference of the detailed microstructure of the ZnO NWs synthesized at different conditions, but more study is required for a quantitative explanation.

The evolution of the piezoresistive coefficient of ZnO NWs is mainly deduced from the cross-sectional shape and size dependence of Young's modulus. This finding sheds light on a new selection strategy of the optimal NW size, especially for the applications that demand high piezoresistivity. A similar strategy was also reported by Rinaldi et al.,[65] from the point of view of piezoelectric effect of ZnO devices. We also note that the cylindrical NWs have lower resistivity than the hexagonal ones, so the shape dependence of Π follows a similar trend as bulk Si:[66] the piezoresistive coefficient increases as the resistivity decreases.

In conclusion, single crystalline ZnO NWs have been fabricated via thermal evaporation without intentional doping. Their cross-sectional geometry can be tuned by adjusting the gas flow rate. Besides clarifying the size effect on Young's modulus, we demonstrated that for NWs with similar diameter, those having hexagonal cross-sectional shape exhibit significantly higher Young's modulus and electrical resistivity than the cylindrical ones. This effect can be attributed to the different density of point defects inherited from the growth stage, as evidenced by the stronger green emission in the PL spectra of the cylindrical NWs. This study offers a new opportunity to tailor the mechanical and mechanoelectrical properties of ZnO NWs at the synthesis stage by controlling and optimizing the growth conditions.

■ ASSOCIATED CONTENT

Supporting Information

The Supporting Information is available free of charge on the ACS Publications website at DOI: 10.1021/acs.nanolett.5b02852.

The methods of nanowire growth, mechanical testing specimen preparation, mechanical data acquisition, and analysis and uncertainty estimation. (PDF)

■ AUTHOR INFORMATION

Corresponding Author

*E-mail: zwshan@mail.xjtu.edu.cn.

Notes

The authors declare no competing financial interest.

■ ACKNOWLEDGMENTS

This work was supported by the National Natural Science Foundation of China (Grant Nos. 51231005, 11132006, 51321003, and 51302207) and the National Basic Research Program of China ("973" Program) (Grant Nos. 2010CB631003 and 2012CB619402). We also appreciate the support from the "111" Project of China (Grant No. B06025). K.C. acknowledges the support from the National Young 1000 Talents Program of China. J.L. acknowledges support by NSF DMR-1120901. The authors would like to thank Xixi Wang for performing the PL experiment.

■ REFERENCES

(1) Wang, Z. L.; Song, J. *Science* **2006**, *312* (5771), 242−6.
(2) Wang, Z. L. *Adv. Funct. Mater.* **2008**, *18* (22), 3553−3567.
(3) Wang, Z. L. *J. Phys. Chem. Lett.* **2010**, *1* (9), 1388−1393.
(4) Yang, Y.; Guo, W.; Qi, J.; Zhang, Y. *Appl. Phys. Lett.* **2010**, *97* (22), 223107.
(5) Zhu, G.; Yang, R.; Wang, S.; Wang, Z. L. *Nano Lett.* **2010**, *10* (8), 3151−5.
(6) Pan, C.; Dong, L.; Zhu, G.; Niu, S.; Yu, R.; Yang, Q.; Liu, Y.; Wang, Z. L. *Nat. Photonics* **2013**, *7* (9), 752−758.
(7) Wang, X.; Zhou, J.; Song, J.; Liu, J.; Xu, N.; Wang, Z. L. *Nano Lett.* **2006**, *6* (12), 2768−72.
(8) Zhou, J.; Gu, Y.; Fei, P.; Mai, W.; Gao, Y.; Yang, R.; Bao, G.; Wang, Z. L. *Nano Lett.* **2008**, *8* (9), 3035−40.
(9) Chen, C.; Shi, Y.; Zhang, Y.; Zhu, J.; Yan, Y. *Phys. Rev. Lett.* **2006**, *96* (7), 075505.
(10) Agrawal, R.; Peng, B.; Gdoutos, E. E.; Espinosa, H. D. *Nano Lett.* **2008**, *8* (11), 3668−74.
(11) He, M.-R.; Shi, Y.; Zhou, W.; Chen, J. W.; Yan, Y. J.; Zhu, J. *Appl. Phys. Lett.* **2009**, *95* (9), 091912.
(12) Xu, F.; Qin, Q.; Mishra, A.; Gu, Y.; Zhu, Y. *Nano Res.* **2010**, *3* (4), 271−280.
(13) Stan, G.; Ciobanu, C. V.; Parthangal, P. M.; Cook, R. F. *Nano Lett.* **2007**, *7* (12), 3691−3697.
(14) Wen, B.; Sader, J.; Boland, J. *Phys. Rev. Lett.* **2008**, *101* (17), 175502.
(15) Zhao, M. H.; Ye, Z.-Z. Z.; Mao, S. X. *Phys. Rev. Lett.* **2009**, *102* (4), 45502.
(16) Ni, H.; Li, X. *Nanotechnology* **2006**, *17* (14), 3591−7.
(17) Song, J.; Wang, X.; Riedo, E.; Wang, Z. L. *Nano Lett.* **2005**, *5* (10), 1954−8.
(18) Desai, A. V.; Haque, M. A. *Sens. Actuators, A* **2007**, *134* (1), 169−176.
(19) Bai, X. D.; Gao, P. X.; Wang, Z. L.; Wang, E. G. *Appl. Phys. Lett.* **2003**, *82* (26), 4806.

DOI: 10.1021/acs.nanolett.5b02852
Nano Lett. 2015, 15, 7886−7892

(20) Hoffmann, S.; Östlund, F.; Michler, J.; Fan, H. J.; Zacharias, M.; Christiansen, S. H.; Ballif, C. *Nanotechnology* **2007**, *18* (20), 205503.
(21) Han, X.; Jing, G.; Zhang, X.; Ma, R.; Song, X.; Xu, J.; Liao, Z.; Wang, N.; Yu, D. *Nano Res.* **2009**, *2* (7), 553−557.
(22) Cuenot, S.; Frétigny, C.; Demoustier-Champagne, S.; Nysten, B. *Phys. Rev. B: Condens. Matter Mater. Phys.* **2004**, *69* (16), 165410.
(23) Agrawal, R.; Peng, B.; Espinosa, H. D. *Nano Lett.* **2009**, *9* (12), 4177−83.
(24) Espinosa, H. D.; Bernal, R. A.; Filleter, T. *Small* **2012**, *8* (21), 3233−52.
(25) Liao, L.; Lu, H. B.; Li, J. C.; Liu, C.; Fu, D. J.; Liu, Y. L. *Appl. Phys. Lett.* **2007**, *91*, 173110.
(26) Wang, J.; An, X.; Li, Q.; Egerton, R. F. *Appl. Phys. Lett.* **2005**, *86* (20), 201911.
(27) McCluskey, M. D.; Jokela, S. J. *J. Appl. Phys.* **2009**, *106* (7), 071101.
(28) Oh, Y.; Cyrankowski, E.; Shan, Z.; Asif, S. A. S. Micro/nano-mechanical test system employing tensile test holder with push-to-pull transformer. U.S. Patent 20100095780 A1, 2010.
(29) Wagner, R. S.; Ellis, W. C. *Appl. Phys. Lett.* **1964**, *4* (5), 89.
(30) Yang, P.; Yan, H.; Mao, S.; Russo, R.; Johnson, J.; Saykally, R.; Morris, N.; Pham, J.; He, R.; Choi, H. J. *Adv. Funct. Mater.* **2002**, *12* (5), 323.
(31) Arya, S. K.; Saha, S.; Ramirez-Vick, J. E.; Gupta, V.; Bhansali, S.; Singh, S. P. *Anal. Chim. Acta* **2012**, *737*, 1−21.
(32) Patra, M. K.; Manzoor, K.; Manoth, M.; Vadera, S. R.; Kumar, N. *J. Lumin.* **2008**, *128* (2), 267−272.
(33) Guo, H.; Chen, K.; Oh, Y.; Wang, K.; Dejoie, C.; Syed Asif, S. A.; Warren, O. L.; Shan, Z. W.; Wu, J.; Minor, A. M. *Nano Lett.* **2011**, *11* (8), 3207−13.
(34) Dai, S.; Zhao, J.; He, M. R.; Wang, X.; Wan, J.; Shan, Z.; Zhu, J. *Nano Lett.* **2015**, *15* (1), 8−15.
(35) Coskun, C.; Gedik, N.; Balci, E. *Semicond. Sci. Technol.* **2006**, *21* (12), 1656.
(36) He, J. H.; Ke, J. J.; Chang, P. H.; Tsai, K. T.; Yang, P. C.; Chan, I. M. *Nanoscale* **2012**, *4* (11), 3399−404.
(37) Kuang, Q.; Lao, C.; Wang, Z. L.; Xie, Z.; Zheng, L. *J. Am. Chem. Soc.* **2007**, *129* (19), 6070−1.
(38) Kiasari, N. M.; Soltanian, S.; Gholamkhass, B.; Servati, P. *MRS Online Proc. Libr.* **2012**, *1439*, 139−144.
(39) Soci, C.; Zhang, A.; Xiang, B.; Dayeh, S. A.; Aplin, D. P. R.; Park, J.; Bao, X. Y.; Lo, Y. H.; Wang, D. *Nano Lett.* **2007**, *7* (4), 1003−1009.
(40) Yang, Y.; Wang, G.; Li, X. *Nano Lett.* **2011**, *11* (7), 2845−8.
(41) Zang, J.; Bao, L.; Webb, R. A.; Li, X. *Nano Lett.* **2011**, *11* (11), 4885−9.
(42) Shan, Z. W.; Adesso, G.; Cabot, A.; Sherburne, M. P.; Asif, S. A.; Warren, O. L.; Chrzan, D. C.; Minor, A. M.; Alivisatos, A. P. *Nat. Mater.* **2008**, *7* (12), 947−52.
(43) Liu, B. Y.; Wang, J.; Li, B.; Lu, L.; Zhang, X. Y.; Shan, Z. W.; Li, J.; Jia, C. L.; Sun, J.; Ma, E. *Nat. Commun.* **2014**, *5*, 3297.
(44) Barlian, A. A.; Park, W. T.; Mallon, J. R., Jr.; Rastegar, A. J.; Pruitt, B. L. *Proc. IEEE* **2009**, *97* (3), 513−552.
(45) Cao, J. X.; Gong, X. G.; Wu, R. Q. *Phys. Rev. B: Condens. Matter Mater. Phys.* **2007**, *75* (23), 233302.
(46) Kröger, F. A.; Vink, H. J. *J. Chem. Phys.* **1954**, *22* (2), 250−252.
(47) Kasai, P. H. *Phys. Rev.* **1963**, *130* (3), 989−995.
(48) Vanheusden, K.; Seager, C. H.; Warren, W. L.; Tallant, D. R.; Voigt, J. A. *Appl. Phys. Lett.* **1996**, *68* (3), 403.
(49) Vanheusden, K.; Warren, W. L.; Seager, C. H.; Tallant, D. R.; Voigt, J. A.; Gnade, B. E. *J. Appl. Phys.* **1996**, *79* (10), 7983.
(50) Pan, Y.; Zheng, W. T.; Guan, W. M.; Zhang, K. H.; Yu, S. S.; Hu, X. Y. *Comput. Mater. Sci.* **2014**, *82*, 12−16.
(51) Studenikin, S. A.; Golego, N.; Cocivera, M. *J. Appl. Phys.* **1998**, *84* (4), 2287.
(52) Banerjee, D.; Lao, J. Y.; Wang, D. Z.; Huang, J. Y.; Steeves, D.; Kimball, B.; Ren, Z. F. *Nanotechnology* **2004**, *15* (3), 404−409.
(53) Li, Y.; Meng, G. W.; Zhang, L. D.; Phillipp, F. *Appl. Phys. Lett.* **2000**, *76* (15), 2011.
(54) Wu, X. L.; Siu, G. G.; Fu, C. L.; Ong, H. C. *Appl. Phys. Lett.* **2001**, *78* (16), 2285.
(55) Janotti, A.; Van de Walle, C. G. *Rep. Prog. Phys.* **2009**, *72* (12), 126501.
(56) Oba, F.; Choi, M.; Togo, A.; Tanaka, I. *Sci. Technol. Adv. Mater.* **2011**, *12* (3), 034302.
(57) Duncan, K. L.; Wang, Y.; Bishop, S. R.; Ebrahimi, F.; Wachsman, E. D. *J. Am. Ceram. Soc.* **2006**, *89* (10), 3162−3166.
(58) Kuo, J.-K.; Huang, P.-H.; Wu, W.-T.; Lu, C.-M. *Appl. Phys. A: Mater. Sci. Process.* **2014**, *114* (4), 1247−1256.
(59) Guemmaz, M.; Mosser, A.; Parlebas, J. C. *J. Electron Spectrosc. Relat. Phenom.* **2000**, *107* (1), 91−101.
(60) Xi, J.; Zhang, P.; He, C.; Zang, H.; Guo, D.; Li, T. *Nucl. Instrum. Methods Phys. Res., Sect. B* **2015**, *356*−*357*, 62−68.
(61) Guemmaz, M.; Mosser, A.; Ahuja, R.; Parlebas, J. C. *Int. J. Inorg. Mater.* **2001**, *3* (8), 1319−1321.
(62) Jhi, S.-H.; Louie, S. G.; Cohen, M. L.; Ihm, J. *Phys. Rev. Lett.* **2001**, *86* (15), 3348−3351.
(63) Wang, Y.; Duncan, K.; Wachsman, E.; Ebrahimi, F. *Solid State Ionics* **2007**, *178* (1−2), 53−58.
(64) Wang, G.; Li, X. *Appl. Phys. Lett.* **2007**, *91* (23), 231912.
(65) Rinaldi, A.; Araneo, R.; Celozzi, S.; Pea, M.; Notargiacomo, A. *Adv. Mater.* **2014**, *26* (34), 5976−85.
(66) He, R.; Yang, P. *Nat. Nanotechnol.* **2006**, *1* (1), 42−6.

DOI: 10.1021/acs.nanolett.5b02852
Nano Lett. 2015, 15, 7886−7892

Supplementary Materials for "Growth conditions control the elastic and electrical properties of ZnO nanowires"

Xiaoguang Wang [1], Kai Chen [1], Yongqiang Zhang [1], Jingchun Wan [1], Oden L. Warren [2], Jason Oh [2], Ju Li [1,3], Evan Ma [1,4], Zhiwei Shan [1]

1. Center for Advancing Materials Performance from the Nanoscale (CAMP-Nano) & Hysitron Applied Research Center in China (HARCC), State Key Laboratory for Mechanical Behavior of Materials, Xi'an Jiaotong University, Xi'an 710049, P. R. China

2. Hysitron Incorporated, 9625 West 76th St, Minneapolis, MN, 55344, USA

3. Department of Nuclear Science and Engineering and Department of Materials Science and Engineering, Massachusetts Institute of Technology, Cambridge, Massachusetts 02139, USA

4. Department of Materials Science and Engineering, The Johns Hopkins University, Baltimore, Maryland 21218, USA

1. The Schematic diagram of the three-probe configuration

In the so-called three-point measurement configuration, in fact four metallic leads were made and connected to the four existing electrodes, as shown in Figure S1a. No electric current passed through R_{c3} and R_{c4} during the measurement, so the contact resistance was ruled out. The equivalent circuit of such three-point configuration is shown in Figure S1b, which can be clearly found to be equivalent to the conventional four-point measurement.

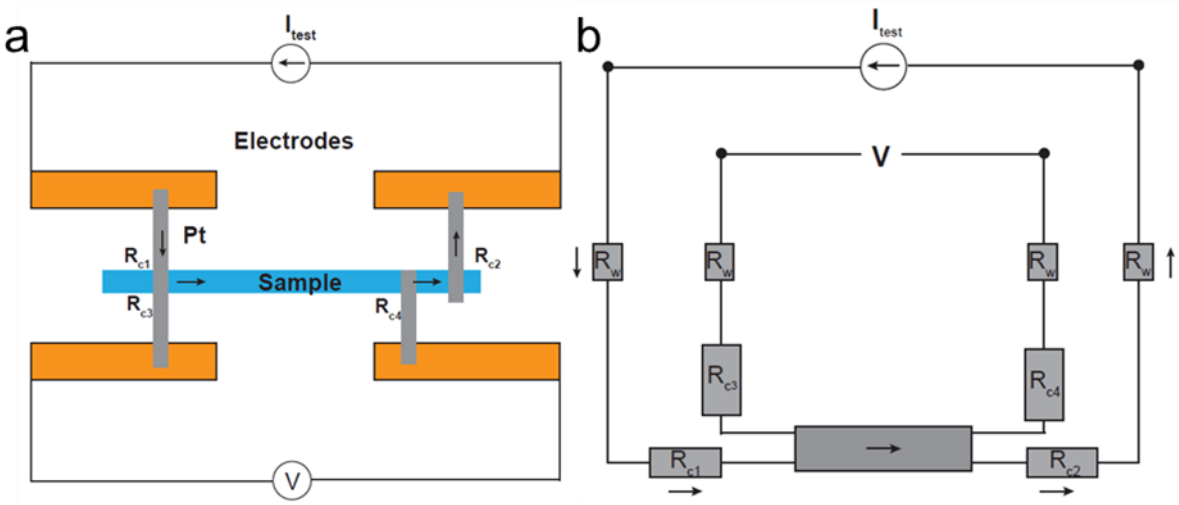

Figure S1 | Schematic diagram of the three-probe configuration. (a) The setup of the three-probe configuration. (b) Equivalent circuit of the three-probe configuration.

2. The stress-strain curves of ZnO NWs

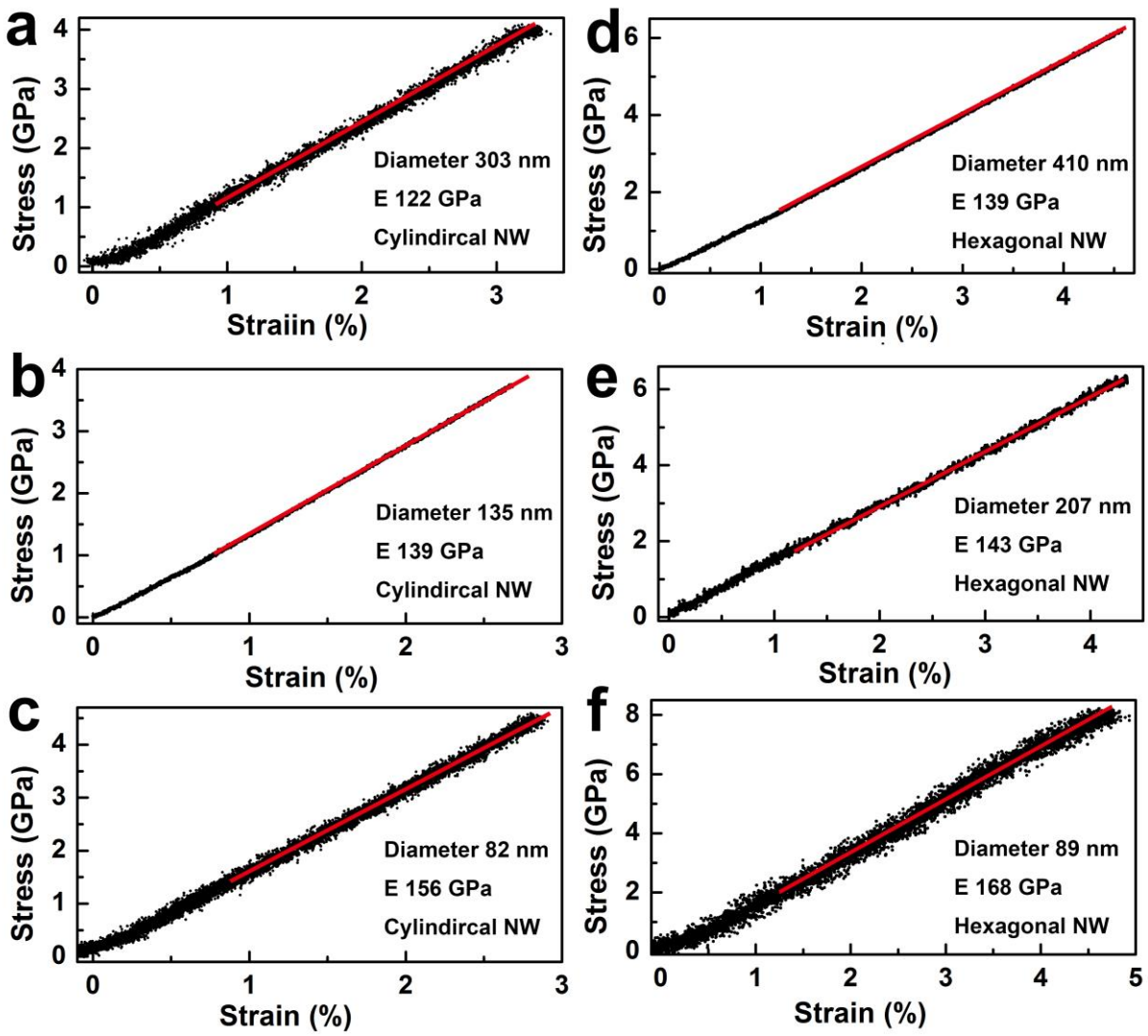

Figure S2 | The stress-strain curves of ZnO NWs of different diameters and cross sectional shapes. The linear part of the curves was fitted and demonstrated as the red lines to obtain the Yong's modulus of each NW. Some of the red lines did not pass the original point because the corresponding NWs were bent slightly during the sample preparation.

3. The fracture strength of ZnO NWs

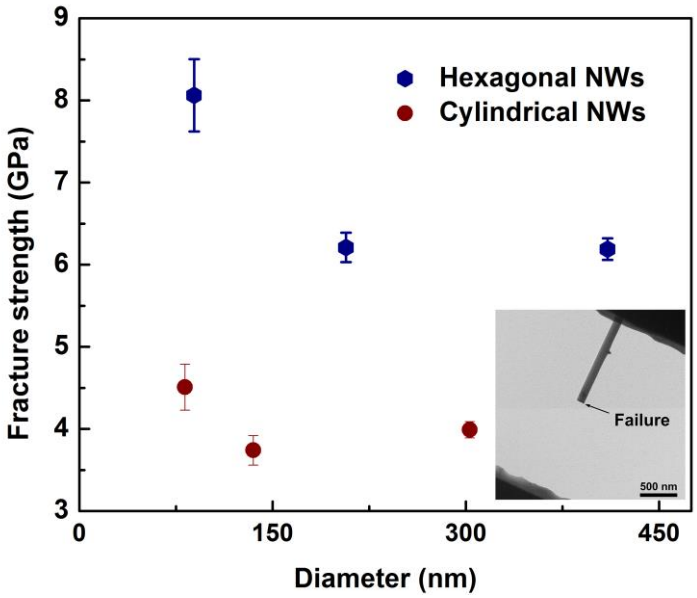

Figure S3 | The fracture strength of ZnO NWs as a function of effective diameters and cross-sectional morphologies. All the NWs showed a brittle fracture behavior as displayed in the inset. The fracture strength of hexagonal NWs is significantly higher than the one of the cylindrical NWs, for the cylindrical NWs contain more defects.

4. The growth of ZnO NWs

Thermal evaporation process was employed to grow the ZnO NWs in a horizontal vacuum tube furnace (Carbolite CTF 17/300)[1, 2]. Mixed powder of ZnO and graphite with a weight ratio of 1:1 was loaded in an alumina boat as the source and placed at the center of the tube furnace. Si (100) wafers cut to ~1.5 cm×0.5 cm and sputter coated with a 10 nm thick Au catalytic thin film were mounted 3-5 mm above the ceramic boat, with the Au film facing the mixed powder. After evacuating the tube to ~0.1 Pa and filling with Ar to atmosphere pressure, the chamber temperature was raised to 925 ^{o}C at the rate of 15 ^{o}C /min under constant flow of pure Ar (100 sccm). In the second stage, a gas mixture of Ar and O_2 with molecular ratio of 10:3 was introduced into the system when the temperature was kept at 925 ^{o}C for 20 minutes. A total gas flow rate of either 130 sccm (Condition 1, for cylindrical ZnO NWs) or 65 sccm (Condition 2,

for hexagonal ZnO NWs) was maintained throughout the experiment. The morphology of the as-synthesized ZnO NWs was studied with field emission SEM (Hitachi U6600).

5. Mechanical testing specimen preparation

The ZnO NWs were first transferred to a copper TEM grid by rubbing the Si substrate on which the NWs were grown. A NW with suitable diameter and length was then positioned on the E-PTP device using a piezoelectric nanomanipulator manufactured by Kleindiek. The NW was aligned carefully perpendicular to the trench edge to secure the uniaxial loading condition. The NW was welded to the E-PTP device via i-beam induced deposition of Pt for mechanical measurement. To minimize damage caused by Ga ion irradiation, only the Pt welded parts were exposed to the ion beam. The whole process was performed inside a FEI Helios 600 NanoLab Dual Beam System.

6. Mechanical data acquisition and analysis

The raw displacement data recorded the motion of the diamond punch of the indenter, which included not only the extension of the NW but also the deformation of the two Pt welds and the semicircular end of the E-PTP device, on which the force was applied from the diamond punch. Therefore, to measure the strain of the NW, two sharp carbon markers (displayed in Figure 3a) were deposited on the surface of NW with the assistance of e-beam[3]. The distance between the two markers before and during the tensile loading was measured from a real-time video, and thus the uniaxial strain was calculated. It is noticed that the strain on the NW could be measured accurately this way as long as there was no strain gradient or localization in the NW. Since the distance was obtained from TEM images, the measurement accuracy depends on the pixel size of

the images. To calculate the stress imposed on the NW, the cross-sectional area and force were measured, respectively. Cross-sectional area was measured in SEM by attaching the fractured NWs to a nano-manipulator tungsten needle and rotating it to parallel with the e-beam (inset of Figure 3b). The net force loaded on the NW was calculated by subtracting the force contributed from the empty E-PTP device from the force read from the transducer of the PicoIndenter system.

7. Uncertainty estimation

The propagation of uncertainties into the measured and calculated quantities was estimated[4]. The Young's modulus E under uniaxial loading is calculated from the following equation:

$$E = \frac{\sigma}{\varepsilon} = \frac{F/A}{\delta/L} \tag{1}$$

where F, A, δ, and L are the NW loading force, NW cross-sectional area, measured displacement of the two carbon marks and initial distance between the marks, respectively. Since the area and distance were measured from TEM images or real-time video, the measurement accuracy depended on the pixel size of the images. The force error came from instrumental error of the transducer of the holder. Thus the propagated percentage uncertainty ΔE into E can be estimated by

$$\frac{\Delta E}{E} = \sqrt{\left(\frac{\Delta F}{F}\right)^2 + \left(\frac{\Delta A}{A}\right)^2 + \left(\frac{\Delta \delta}{\delta}\right)^2 + \left(\frac{\Delta L}{L}\right)^2} \tag{2}$$

where ΔF, ΔA, $\Delta \delta$, and ΔL are the measurement uncertainty of NW unloading force, NW cross-sectional area, displacement of the two carbon marks and initial distance between the marks, respectively.

REFERENCES

1. Kuo, T.-J.; Lin, C.-N.; Kuo, C.-L.; Huang, M. H. *Chemistry of Materials* 2007, 19, (21), 5143-5147.

2. Wang, J.; An, X.; Li, Q.; Egerton, R. F. *Applied Physics Letters* 2005, 86, (20), 201911.

3. Tian, L.; Cheng, Y.-Q.; Shan, Z.-W.; Li, J.; Wang, C.-C.; Han, X.-D.; Sun, J.; Ma, E. *Nature Communications* 2012, 3, 609.

4. Taylor, J. R., *An Introduction to Error Analysis: The Study of Uncertainties in Physical Measurements*. University Science Books: 1997.